

DarSwin : Distortion-Aware Radial Swin Transformers for Wide Angle Image Recognition

Akshaya Athwale^{1*†}, Ichrak Shili^{1*†}, Émile Bergeron¹, Arman Afrasiyabi³,
Justin Lagüe¹, Ola Ahmad², Jean-François Lalonde¹

¹Université Laval.

²Thales Digital Solutions.

³Yale University.

*Corresponding author(s). E-mail(s): akshaya.athwale.1@ulaval.ca; ichrak.shili.1@ulaval.ca;

†These authors contributed equally to this work.

Abstract

Wide-angle lenses are commonly used in perception tasks requiring a large field of view. Unfortunately, these lenses produce significant distortions, making conventional models that ignore the distortion effects unable to adapt to wide-angle images. In this paper, we present a novel transformer-based model that automatically adapts to the distortion produced by wide-angle lenses. Our proposed image encoder architecture, dubbed DarSwin, leverages the physical characteristics of such lenses analytically defined by the radial distortion profile. In contrast to conventional transformer-based architectures, DarSwin comprises a radial patch partitioning, a distortion-based sampling technique for creating token embeddings, and an angular position encoding for radial patch merging. Compared to other baselines, DarSwin achieves the best results on different datasets with significant gains when trained on bounded levels of distortions (very low, low, medium, and high) and tested on all, including out-of-distribution distortions. While the base DarSwin architecture requires knowledge of the radial distortion profile, we show it can be combined with a self-calibration network that estimates such a profile from the input image itself, resulting in a completely uncalibrated pipeline. Finally, we also present DarSwin-Unet, which extends DarSwin to an encoder-decoder architecture suitable for pixel-level tasks. We demonstrate its performance on depth estimation and show through extensive experiments that DarSwin-Unet can perform zero-shot adaptation to unseen distortions of different wide-angle lenses.

1 Introduction

Wide field of view (FOV) lenses are becoming increasingly popular because their increased FOV minimizes cost, energy, and computation since fewer cameras are needed to image the entire environment. They are having a positive impact on many applications, including security [1], augmented reality (AR) [2], healthcare and more particularly, autonomous vehicles [3, 4], which require sensing their surrounding 360° environment.

Unfortunately, such wide-angle lenses create significant distortions in the image since the perspective projection model no longer applies: straight lines appear curved, and the appearance of the same object changes as a function of its position on the image plane. This distortion breaks the translation equivariance assumption implicit in convolution neural networks (CNNs) and, therefore, limits their applicability. This problem is further exacerbated by the diversity in lens distortion profiles: as we will demonstrate, a network naively trained for a specific lens tends to overfit to that

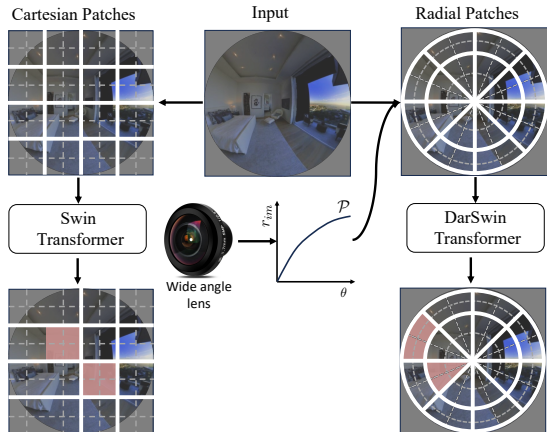


Fig. 1: Illustration of (cartesian) Swin [5] (left) and our (radial) DarSwin (right) given a wide-angle image (middle). While Swin [5] computes attention on the pre-defined windows over square image patches (bottom left orange region), DarSwin performs radial transformations using distortion-aware radial patches and computes the attention on windows defined over radial patches (shown in orange region bottom right), which enables greater generalization capabilities across different lenses.

specific distortion and does not generalize well when tested on another lens. Just as methods are needed to address the “domain gap” [6] from dataset bias [7, 8], we believe we must also bridge the “distortion gap” to truly make wide-angle imaging applicable.

One popular strategy to bridge the distortion gap is to cancel the effect of distortion on the image plane by warping the input image back to a perspective projection model according to calibrated lens parameters. Conventional approaches can then be trained and tested on the resulting “un-distorted” images. A wide array of such methods, ranging from classical [9–13] to deep learning [14, 15], have been proposed. Unfortunately, warping a very wide angle image to a perspective projection tends to create severely stretched images and restricts the maximum field of view since, in the limit, a point at 90° azimuth projects at infinity. Reducing the maximum field of view defeats the purpose of using a wide-angle lens in the first place. Other projections are also possible (e.g., cylindrical [16], or piecewise linear [4]), but these also tend to create unwanted distortions or suffer from resolution loss.

Recently, methods that break free from the “undistort first” strategy aim to reason directly about the

images without undistorting them. For example, methods like [17, 18] use deformable convolutions [19, 20] to adapt convolution kernels to the lens distortion. However, the high computational cost of deformable CNNs constrains the kernel adaptation to a few layers inside the network. Other approaches like spherical CNNs [21] or gauge equivariant CNN [22] can adapt to different manifolds, but their applicability for lens distortion has not been demonstrated. Finally, vision transformers [23] and their more recent variants [5, 24, 25] could also better bridge the “distortion gap” since they do not assume any prior structure other than permutation equivariance, but their cartesian partitioning of the image plane does not take lens geometry into account (see fig. 1).

In this paper, we present DarSwin, a transformer-based image encoder architecture that adapts its structure to the lens distortion profile, which is assumed to be known (calibrated lens). Our method, inspired by the recent Swin transformer architecture [5], leverages a distortion-aware sampling scheme for creating token embeddings, employs polar patch partitioning and merging strategies, and relies on angular relative positional encoding. This explicitly embeds knowledge of the lens distortion in the architecture and makes it much more robust to the “distortion gap” created by training and testing on different lenses. We show, through extensive classification experiments, that DarSwin can perform zero-shot adaptation (without pretraining) across different lenses compared to the baselines Swin [5] trained on distorted and undistorted images and DAT [25] trained on distorted images.

While the DarSwin encoder architecture was originally introduced in [26], this paper significantly extends the original contribution in three main ways. First, we show that, by combining a DarSwin encoder with another network that estimates the lens distortion from the image, we can remove the need for calibrating the lens profile, resulting in an entirely uncalibrated pipeline. Second, we extend the DarSwin encoder to a full encoder-decoder distortion-aware architecture, DarSwin-Unet, suitable for per-pixel prediction tasks. Third, we present experiments on the depth estimation task, which show that DarSwin-Unet is much more robust to changes in lens distortions at test time than all of the compared baselines, including Swin-Unet [27] and Swin-UPerNet [5, 28] trained on both distorted and undistorted images, and DAT-UPerNet [25, 28] trained on distorted images.

2 Related work

Panoramic distortion

Panoramic images span the full 360° field of view and are most commonly projected onto a plane using an equirectangular projection. This projection introduces significant distortions, especially near the poles. Many works have explicitly designed approaches to deal with equirectangular distortion, to perform different downstream tasks like depth estimation [29], saliency detection [30], segmentation [31], layout estimation [32], and object detection [33] to name a few. However, these are specifically designed for equirectangular distortion and do not generalize to wide-angle lenses.

Image undistortion

Establishing image and object recognition tasks from wide-angle cameras directly is relatively recent [4, 16, 34–36] due to the presence of distortions in the image. In computer vision, the application of wide-angle images ranges from visual perception [37] to autonomous vehicle cameras [4, 38, 39]. In this respect, the initial studies mainly focused on correcting the distortion of the image [11, 14, 15, 40–46]. Many methods like [42, 43, 47] use a distortion distribution map to correct distortion. Distortion correction can lead to multiple types of sampling artifacts, as explained in [4], leading to a performance loss. In contrast, DarSwin relies on distortion parameters and reasons directly on wide-angle images.

Convolution-based approaches

CNNs [48–50] are particularly well-suited for perspective images due to their implicit bias and translational equivariance [51]. Methods like [34, 35, 52] try to adapt CNNs on fisheye images for tasks such as object detection. However, the distortion caused by wide-angle images breaks this symmetry, which reduces the generalization performance of CNNs. Methods like [53–56] use self-supervised learning combined with techniques like distillation or multi-task learning to have a better understanding of distortion. Deformable convolutions [19] (later extended in [20]) learn a deformation to be applied to convolution kernels, which can provide greater flexibility at the cost of significant additional computation. Closer to our work, [3, 17, 18, 57] use such deformable CNNs to understand the distortion in a fisheye image. In contrast, DarSwin leverages attention-based mechanisms rather than convolution.

Self-attention-based approaches

Vision transformers (ViT) [23] use self-attention mechanisms [58] computed on image patches rather than performing convolutions. Unlike CNNs, a ViT does not have a fixed geometric structure in its architecture: any extra structure is given via positional encoding. More recently, the Swin transformer architecture [5] proposes a multi-scale strategy of window-based attention. Later, deformable attention transformer (DAT) [25], adapts the concept of deformable CNNs [19, 20] to increase adaptability. [59] proposes a distortion-aware architecture using a transformer network, but the network is limited to a fixed equirectangular distortion. In contrast, DarSwin adapts its structure to the lens distortion, which may vary across lenses.

Hybrid-network based approaches

Some methods leverage properties from both self-attention and convolutions and build hybrid networks. Methods like [60] use hybrid networks and try to leverage the geometric property of fisheye images (i.e., the orthogonal placement of objects) and propose a new representation of fisheye road scenes, invariant to the camera viewing direction. Shi et al. [61] leverages the radial nature of distortion by including polar cross attention for inpainting, but unlike DarSwin, they do not use the lens information in their network. Similar to our method, [54, 56, 62, 63] propose a camera-aware depth estimation network to handle the severe distortion of fisheye cameras: [54] encode the camera intrinsic parameters as a tensor; and [63] propose a self-supervised depth estimation method which relies on the lens distortion parameter for forward and back-projection functions. Both these methods use distortion parameters as a part of the input or training process, but they rely on convolutions whose generalization capabilities are limited due to the translational invariance assumption being broken in wide-angle images. Indeed, the network weights each pixel and its corresponding lens distortion prior equally regardless of the severity of distortion, which affects the ability to generalize to a variety of lens distortion. Hence, [54] shows generalization to lens distortion closer to training distortion, and [63] does not show any generalization results. In contrast, our approach uses the lens parameters to adapt the structure of the input explicitly, weighting each part of the image according to the severity of lens distortion. Hence, we show generalization to a vast range of distortion parameters.

3 Image formation

We begin with a brief review of lens distortion models relevant to this work. The pixel coordinates \mathbf{p}_{im} of a 3D point $\mathbf{p}_w = [x, y, z]^T$ in world coordinates are given by

$$\mathbf{p}_{\text{im}} = [u, v]^T = \mathcal{P}(\mathbf{p}_w), \quad (1)$$

where \mathcal{P} is a 3D-to-2D projection operator, including conversion from homogeneous coordinates to 2D. Here, without loss of generality, the camera is assumed to be at the world origin (so its rotation and translation are ignored).

To represent wide-angle images, it is common practice to use a projection model that describes the relationship between the radial distance $r_{\text{im}} = \sqrt{u^2 + v^2}$ from the image center and the incident angle $\theta = \arctan(\sqrt{x^2 + y^2}/z)$. This relationship takes the generic form

$$r_{\text{im}} = \mathcal{P}(\theta). \quad (2)$$

Within the scope of our interest, we consider three types of projections.

Perspective projection.

Under the perspective projection model, the projection operator \mathcal{P} takes the form [13]

$$\mathcal{P}_{\text{pers}}(\theta) \equiv r_{\text{im}} = f \tan(\theta), \quad (3)$$

where f is the focal length (in pixels). The perspective projection is the rectilinear model of pinhole lenses. Wide-angle lenses disobey the law of perspective projection and therefore cause non-linear distortions.

Polynomial projection.

In the case of wide-angle lenses, there are several classical projection models [64–67] giving different formulas for \mathcal{P} ; see [68] for a detailed analysis of the accuracy of such models. A unified, more general, model is defined as an n -degree polynomial and given by

$$\mathcal{P}_{\text{poly}}(\theta) \equiv r_{\text{im}} = a_1\theta + a_2\theta^2 + \dots + a_n\theta^n. \quad (4)$$

For example, the WoodScape dataset [4] employs a 4-degree ($n = 4$) polynomial for their lens calibration. We adopt this polynomial function to define the lens projection curve used in our method (sec. 4).

Spherical projection.

The spherical projection model [69, 70] or unified camera model describes the radial distortion by a *single, bounded* parameter $\xi \in [0, 1]^1$. It projects the world point \mathbf{p}_w to the image as follows

$$[u, v]^T = \left[\frac{xf}{\xi\|\mathbf{p}_w\| + z}, \frac{yf}{\xi\|\mathbf{p}_w\| + z} \right]^T. \quad (5)$$

We employ this model in experiments (sec. 5) because of its ability to represent distortion with a single parameter.

4 Methodology

4.1 Overview

fig. 2 shows an overview of our distortion-aware transformer model. This model extends the encoder architecture (DarSwin), proposed in [26] for classification tasks, to the new DarSwin-Unet architecture that scales up to pixel-level tasks. The encoder (DarSwin) accepts as input a single image and its distortion parameters in the form of a lens projection curve $\mathcal{P}(\theta)$ (see eq. (2)). The image is first segmented into patches according to a polar partitioning module (sec. 4.2). Then, a linear embedding is computed from sampled points (sec. 4.3), reshaped into a radial-azimuth projection and fed to the first Swin transformer block. The attention mechanism employs an angular relative positional encoding scheme guided by the lens curve (sec. 4.5). This is followed by three blocks performing patch merging (sec. 4.6) and additional Swin transformer blocks. The decoder employs similar transformer blocks along with azimuth patch expanding layer for upsampling (sec. 4.7). A k -NN layer (sec. 4.8) then projects the feature map from polar to cartesian space and is followed by a final linear projection layer. More details on each of these steps are provided below.

4.2 Polar partition

The first step of our proposed architecture is to partition the image domain into patches. As opposed to Swin, which performs the split in cartesian coordinates (fig. 3a), DarSwin employs a polar patch partitioning strategy (fig. 3b). After centering a polar coordinate system on the image center (assumed to be known), we

¹ ξ can be slightly greater than 1 for certain types of catadioptric cameras [71] but this is ignored here.

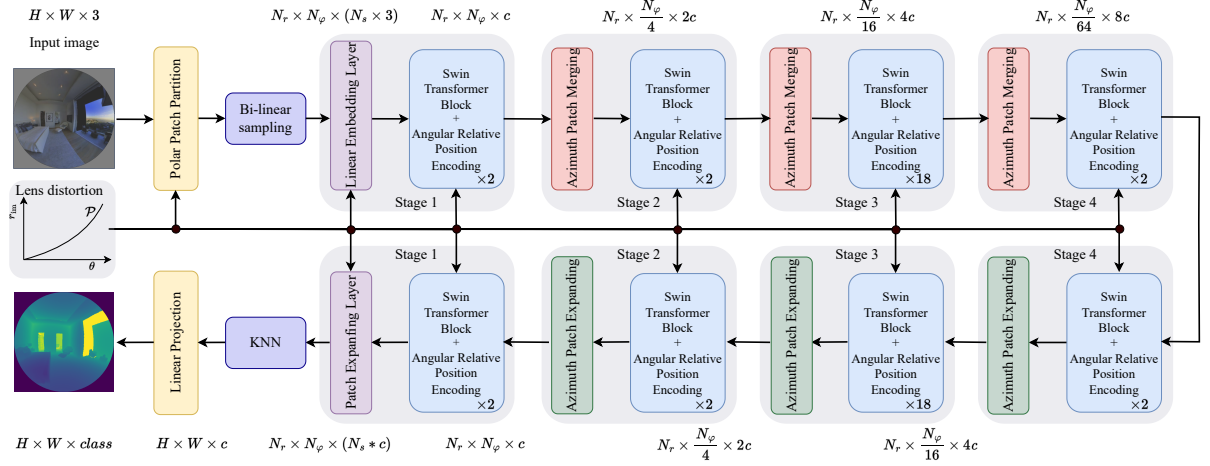


Fig. 2: Overview of our distortion aware transformer unet architecture, DarSwin-UNet which. It employs hierarchical layers of DarSwin’s transformer blocks [26] (top row) and is inspired by unet architecture from Swin-UNet [27]. To make it adapt to lens distortion, the patch partition, linear embedding, and patch merging layers and patch expanding layer all take the lens projection curve \mathcal{P} (c.f. sec. 3) as input similar to DarSwin. The k -NN layer is used to project the feature map from polar ($N_r \times N_\varphi$) to cartesian space $H \times W$.

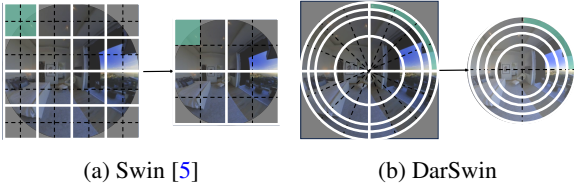


Fig. 3: Illustration of the difference between (a) Swin [5], which uses Cartesian image patches (shown in grey) and windows (shown in white borders) by making divisions along image axes, Swin performs attention on a Cartesian window and merges 2×2 neighbourhood patches to build a hierarchical structure (shown in the green and orange shaded region) (b) our proposed DarSwin uses polar image patches by making divisions along radius and azimuth. In our case, the images patches (shown in grey) and windows (shown in white borders) are defined along azimuth and merged along azimuth as (shown in the green and orange shaded region)

first split according to azimuth angle φ in N_φ equiangular regions. For the radial dimension, we split the image into N_r radial regions such that the splits are equiangular in θ and obtain the corresponding image-space radii using the lens projection function $\mathcal{P}(\theta)$ (see eq. (2)). The total number of patches is therefore $N_\varphi \times N_r$. In

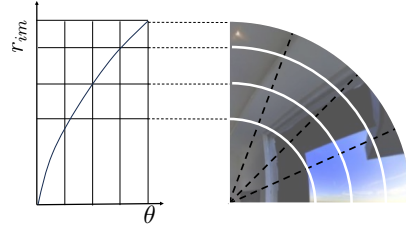


Fig. 4: Example of distortion aware polar patch partition. Here, $N_r = 4$ and $N_\varphi = 4$ partitions along radius and azimuth, respectively, are used to illustrate (right, only the top-right quadrant of the image is shown). While the azimuth partitioning is performed in an equiangular fashion, the radial dimension takes the lens distortion curve (left) into account. The field of view along the incident angle θ is split into N_r equal parts (left), and corresponding radial are obtained from the distortion curve. Hence, for different lenses, we can have different radii depending on the distortion parameters.

our experiments, we set $N_r = 16$ and $N_\varphi = 64$ for an input image of size 64×64 pixels.

4.3 Linear embedding

The resulting image patches created by this approach have an unequal amount of pixels. Therefore, we rely on a distortion aware sampling strategy to obtain the

same number of points for each patch. To sample from the images, we define the number of sampling points along the radius and azimuth, as shown in fig. 5, and adapt the pattern according to each partition. In our experiments, we set 10 sampling points along the radius and azimuth for each patch. Points are sampled in an equiangular fashion along the azimuth direction. For the radial dimension, we sample according to the same pattern as the polar partitioning (sec. 4.2); that is, we split in an equiangular fashion according to θ and obtain the corresponding image-space radii using $\mathcal{P}(\theta)$ (eq. (2)). The input image is sampled using bilinear interpolation, and samples are arranged in a polar format, as illustrated in fig. 4. The resulting sample values are then fed into a linear embedding layer to produce token embeddings as input for the subsequent transformer block.

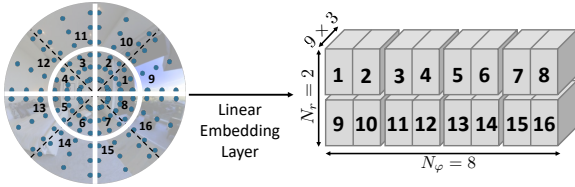


Fig. 5: Example of sampling strategy on patch partitions. For illustration, 16 patches ($N_r = 2$ and $N_\varphi = 8$) are used, with window size (1, 2), i.e. ($M_r = 1, M_\varphi = 2$). RGB values are then sampled bilinearly from the image (6 blue dots per patch) and re-arranged in polar coordinates.

4.4 Window-based self attention

The Swin transformer architecture [5] uses window-based self-attention, where attention is computed on non-overlapping windows of $M \times M$ patches. Here, we maintain that strategy, but the polar nature of our patches allows for an additional design choice: the number of patches along azimuth M_φ and radius M_r can be different. As shown in tab. 1, we define two variants: M patches along both azimuth and radius, $M_r = M_\varphi = M$ (DarSwin-RA); or $M_\varphi = M^2$ patches along azimuth and $M_r = 1$ patch along radius (DarSwin-A). Note that we break this rule when the input resolution across radius or azimuth becomes lower than M to maintain the number of patches in each window equals to M^2 at each stage (see tab. 1).

We experimentally found (see sec. 5.6) that computing attention across M^2 patches along the azimuth (DarSwin-A) yielded improved performance.

Similarly, shifted window self-attention (used in [5] to introduce connections across windows at each stage of the network) is done by displacing the windows by M patches along the azimuth.

4.5 Angular relative positional encoding

The Swin transformer relative positional encoding [5] includes a position bias $B \in \mathbb{R}^{M^2 \times M^2}$, where M^2 is the number of patches in a window, added to each head when computing similarity:

$$\text{Att}(Q, K, V) = \text{Softmax}(QK^T / \sqrt{d} + B)V, \quad (6)$$

where $Q, K, V \in \mathbb{R}^{M^2 \times d}$ are the queries, keys, and values matrices respectively; and d is the query/key dimension.

Since DarSwin follows a radial partitioning, we employ an angular relative positional encoding to capture the relative position between tokens with respect to incident θ and azimuth φ angles. We divide the position bias B in eq. (6) into two parts: B_θ and B_φ , the incident-angular and azimuthal relative position bias respectively. Given the i -th token angular coordinates

$$\theta_i = \frac{\theta_{\max}(i - 0.5)}{N_r} \quad \text{and} \quad \varphi_i = \frac{2\pi(i - 0.5)}{N_\varphi}, \quad (7)$$

where θ_{\max} is the half field of view. The relative angular positions ($\Delta\theta, \Delta\varphi$) between tokens i, j are

$$\begin{aligned} \Delta\theta &= \theta_i - \theta_j, \text{ where } i, j \in [1, \dots, N_\theta], \text{ and} \\ \Delta\varphi &= \varphi_i - \varphi_j, \text{ where } i, j \in [1, \dots, N_\varphi]. \end{aligned} \quad (8)$$

The two tensors B_φ and B_θ are defined as

$$B_\theta = a_{\Delta\theta} \sin(\Delta\theta) + b_{\Delta\theta} \cos(\Delta\theta), \quad (9)$$

$$B_\varphi = a_{\Delta\varphi} \sin(\Delta\varphi) + b_{\Delta\varphi} \cos(\Delta\varphi). \quad (10)$$

Here, a_* and b_* are trainable coefficients. Since the relative positions in a window along angular and azimuth axes ranges from $[-M_\theta + 1, M_\theta - 1]$ and $[-M_\varphi + 1, M_\varphi - 1]$ respectively, where M_θ and M_φ are number of patches in a window (see sec. 4.4, here $M_\theta = M_r$). We parameterize two bias matrices $\hat{B}_\varphi \in \mathbb{R}^{(2M_\varphi - 1) \times 2}$ and $\hat{B}_\theta \in \mathbb{R}^{(2M_\theta - 1) \times 2}$. Hence a_* and b_* for a particular token are sampled from \hat{B}_θ and \hat{B}_φ based on the

relative positions of the said token to generate angular and azimuth position values in B_θ and B_φ .

Finally, the two tensors $B_\theta, B_\varphi \in \mathbb{R}^{M_r^2 \times M_\varphi^2}$ are built on all pairs of tokens. The final attention equation is thus

$$\text{Att}(Q, K, V) = \text{Softmax}(QK^T / \sqrt{d} + B_\theta + B_\varphi)V. \quad (11)$$

4.6 Polar patch merging

Similar to window-based self attention (sec. 4.4), the polar nature of our architecture enables many possibilities when merging patches. For example, we could merge 2×2 neighboring patches (DarSwin-RA) or 1×4 merge along azimuth (DarSwin-A) as shown in tab. 1. We found the azimuth merging strategy to outperform the others in our experiments (see sec. 5.6).

4.7 Polar patch expanding

As in [27], we use an MLP layer for the expanding layer. We use this layer along the azimuth dimension to upsample by a $4 \times$ factor. For example, consider the first patch expanding layer in fig. 2. The input feature map ($N_r \times \frac{N_\varphi}{64} \times 8c$) is first given to an MLP layer to expand the feature dimension by $4 \times$ to get ($N_r \times \frac{N_\varphi}{64} \times 32c$). The feature map is then rearranged to reduce the feature dimension and increase the resolution of feature map along azimuth dimension to obtain ($N_r \times \frac{N_\varphi}{16} \times 4c$).

4.8 k -NN layer

Lastly, we employ a k -NN layer to map the polar feature map back to cartesian coordinates. Each pixel coordinate in the image is associated with its k closest samples (we use $k = 4$), and their respective feature vectors are averaged. Since sample point locations are known, the k -NN layer is fixed and not trainable. The k -NN output (of dimensions $H \times W \times c$) is fed into the last linear projection layer to get the desired output for the required task.

4.9 Data availability

All data supporting the findings of this study are available within the paper and explained in sec. 5.1 and sec. 6.1.

Table 1: Model architecture specification and variants. In both variants, we extend the architecture of DarSwin [26] to DarSwin-Unet, inspired by Swin-Unet [27], which has three stages of patch merging, two stages of bottleneck, and three stages of patch expanding layer. ‘‘Resolution’’: resolution of input feature map at every stage. ‘‘Window Size’’ (M_r, M_φ): Number of patches along radial M_r or azimuth M_φ axis in a window. ‘‘DarSwin-RA’’: encoder architecture variant merging 2×2 neighborhood patches along the radius and azimuth. ‘‘DarSwin-A’’: encoder architecture variant merging 1×4 neighborhood patches along the radius and azimuth. ‘‘ k -NN’’: layer to map the output feature map from polar back to cartesian coordinates.

DarSwin-RA		DarSwin-A	
Resolution	Window Size (M_r, M_φ)	Resolution	Window Size (M_r, M_φ)
Stage-1 (16, 64)	(4, 4)	Stage-1 (16, 64)	(1, 16)
Stage-2 (8, 32)	(4, 4)	Stage-2 (16, 16)	(1, 16)
Stage-3 (4, 16)	(4, 4)	Stage-3 (16, 4)	(4, 4)
Stage-4 (2, 8)	(2, 8)	Stage-4 (16, 1)	(16, 1)
Stage-4 (2, 8)	(2, 8)	Stage-4 (16, 1)	(16, 1)
Stage-3 (4, 16)	(4, 4)	Stage-3 (16, 4)	(4, 4)
Stage-2 (8, 32)	(4, 4)	Stage-2 (16, 16)	(1, 16)
Stage-1 (16, 64)	(4, 4)	Stage-1 (16, 64)	(1, 16)
k -NN (64, 64)	N/A	k -NN (64, 64)	N/A

5 Classification experiments

We begin by evaluating the efficacy of our proposed DarSwin encoder only (i.e., top row of fig. 2). For this, we perform a series of experiments on image classification. Since there exists no classification dataset for wide-angle images, we instead create synthetically distorted images using 200 randomly chosen classes from the ImageNet1k dataset [48].

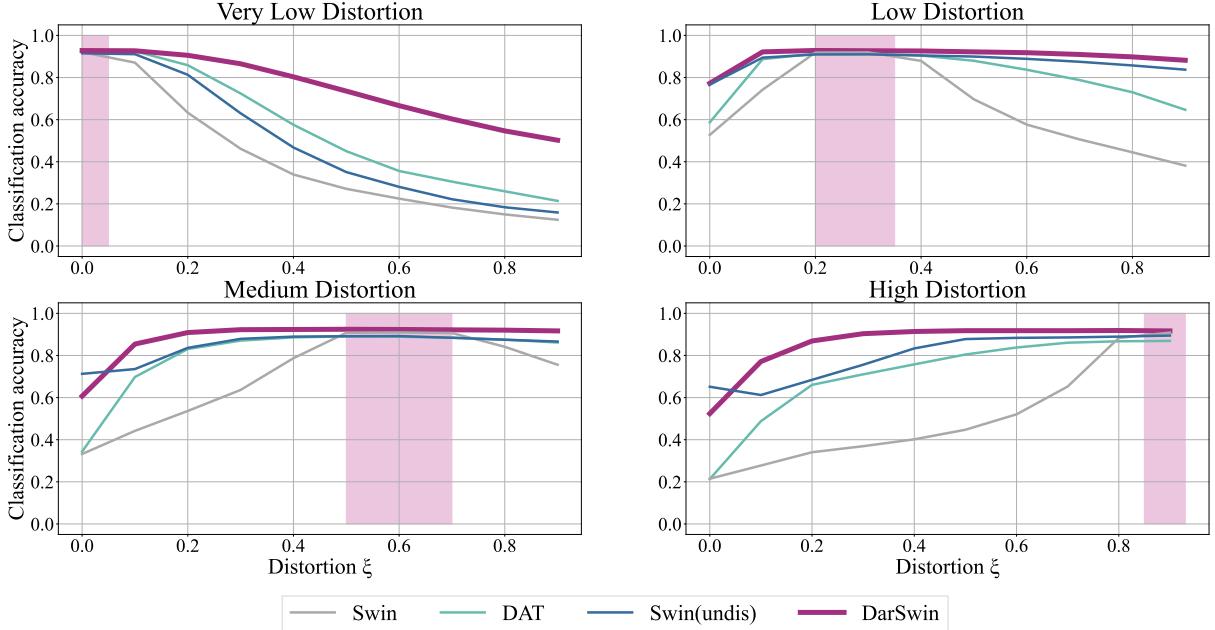


Fig. 6: Mean top-1 classification accuracy as a function of input lens distortion for our method (DarSwin-A) and previous state of the art: DAT [25], Swin [5], and Swin(undis) (see text). All methods are trained on a restricted set of lens distortion curves (indicated by the pink shaded regions), from top-left: very low, low, medium and high distortion. We observe zero-shot adaptation to lens distortion of each approach by testing across all $\xi \in [0, 1]$.

5.1 Dataset

To evaluate our approach on a wide range of conditions, we employ the unified spherical projection model (c.f. sec. 3) to synthetically distort the (perspective) ImageNet1k images. For this, we warp the images at the original pixel resolution (224×224) then downsample to (64×64) for all experiments.

Training sets

We generate four different training sets with different levels of distortion, defined by the distortion parameter ξ : “very low” ($\xi \in [0.0, 0.05]$), “low” ($\xi \in [0.2, 0.35]$), “medium” ($\xi \in [0.5, 0.7]$), and “high” ($\xi \in [0.85, 1.0]$). Fig. 7 shows examples of a checkerboard image distorted at each level. Training images are distorted on-the-fly during training with the distortion level sampled uniformly from the interval mentioned above. Each training set contains 260,000 images and 10,000 validation images, over 200 classes.

Test set

Test sets of 30,000 images over 200 classes are generated using the same procedure. Here, ξ is determined once for each image and kept fixed. We test for all

ξ values between $[0, 1]$ to evaluate generalization to different lens distortions.

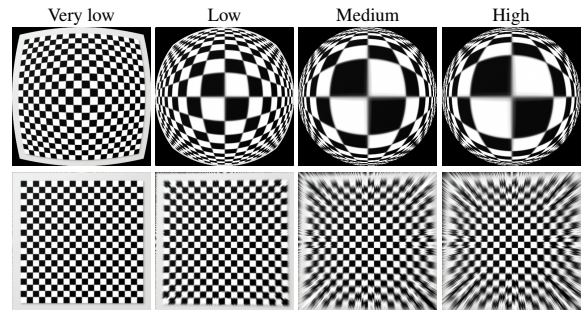


Fig. 7: Visualization of a checkerboard pattern distorted according to each distortion level at its original resolution of ($224, 224$) and downsampled to ($64, 64$) in our four training sets. From left to right: very low, low, medium, and high. The second row represents the respective undistorted images.

5.2 Baselines and training details

We perform classification experiments using DarSwin architecture, which can be obtained by appending a 200-unit linear layer to the output of the stage 4 block of the encoder in fig. 2. We compare our approach with the following baselines: Swin-S [5], Deformable Attention Transformer (DAT-S) [25], and Swin-S on input images that have been undistorted back to a perspective projection (dubbed “Swin(undis)”). As with our DarSwin, this last baseline has knowledge of the distortion parameters, whereas the first two do not. Note that we do not include comparisons to methods that estimate distortion [11, 14, 15, 41]. Indeed, the spherical projection model (sec. 3) is bijective: the undistortion function has a closed form and is exact. Therefore, the Swin (undis) method serves as an upper bound to all self-calibration methods because it is, in essence, being given the “ground truth” undistortion.

All three baselines employ 32 divisions along the image width and height. For DarSwin, we use $N_r = 16$ and $N_\varphi = 64$ divisions along the radius and azimuth respectively, which yields the same total number of 1024 patches for all methods. All three baselines are trained with a window size (4, 4) on our synthetically distorted training sets.

All methods use the AdamW optimizer on a batch size of 128 using a cosine decay learning rate scheduler and 20 epochs of linear warm-up. We use an initial learning rate of 0.001 and a weight decay of 0.05. We include all of the augmentation and regularization strategies of [5], except for random crop and geometric transformation (like shearing and translation). Our model requires 0.03M additional parameters over the Swin baseline, which contains 48M, representing a 0.061% increase.

5.3 Zero-shot generalization

We are interested in evaluating whether our distortion-aware method can better generalize to other unseen lenses at test time. Hence, we train each approach on a specific distortion level (c.f. sec. 5.1) and evaluate them on all distortion values $\xi \in [0, 1]$. For this, the entire test set is distorted using a single ξ value, and we repeat this process for every ξ in uniform discrete interval $[0, 1]$ with step size 10, to simulate different lens distortion.

Results are reported in fig. 6, where the distribution of training distortions is drawn in pink. We observe that DarSwin performs on par with the baselines when test distortions overlap with training, but shows much

Methods	Very Low	Low	Medium	High
DarSwin	80.33	92.61	92.35	91.39
Swin	33.94	87.90	78.7	40.1
Swin (undis)	47.48	91.52	91.07	87.34
DAT	57.5	90.4	88.5	75.7

Table 2: Comparisons of mean top-1 accuracy of the models trained on four levels of distortion (pink regions in fig. 6) and tested on distortion level $\xi = 0.4$. Each row is color-coded as **best** and **second best**.

greater zero-shot generalization capabilities outside of the training lens distortion domain. Furthermore, tab. 2 shows the top-1 accuracy for the test set distorted with $\xi = 0.4$, which is in none of the training intervals. Again, we note that DarSwin yields better generalization accuracy (without fine-tuning) than all baselines, even Swin(undis) which also has access to the ground truth distortion function (see sec. 5.2).

5.4 Sensitivity analysis

Recall that all experiments so far assume knowledge of the ground truth lens distortion parameter, ξ , of each image at both training and test time. We are interested in evaluating the sensitivity of approaches which assume knowledge of the lens distortion curve (namely, DarSwin and Swin(undis)) to errors in ξ at test time. To this end, we inject an error $\Delta\xi \in [-0.4, 0.4]$ during the evaluation of trained models and show the results in fig. 8. As can be observed, DarSwin is overall much more robust to errors in the distortion parameter than Swin(undis). This is especially visible when models are trained on the “very low” group. In this scenario, the accuracy of Swin(undis) severely drops when a small error in ξ is provided to the network. In contrast, the performance of DarSwin remains much more stable across even large values of $\Delta\xi$.

5.5 Self-calibration

Given the robustness of DarSwin to errors in lens distortion curve, we also experiment with combining it with a separate “calibration” network whose task is to estimate the lens distortion parameter ξ from the input image itself.

Training a calibration network

Here, we follow the same approach as [72] and employ a ConvNext [73] encoder and replace the last layer with a linear layer which predicts the distortion ξ directly.

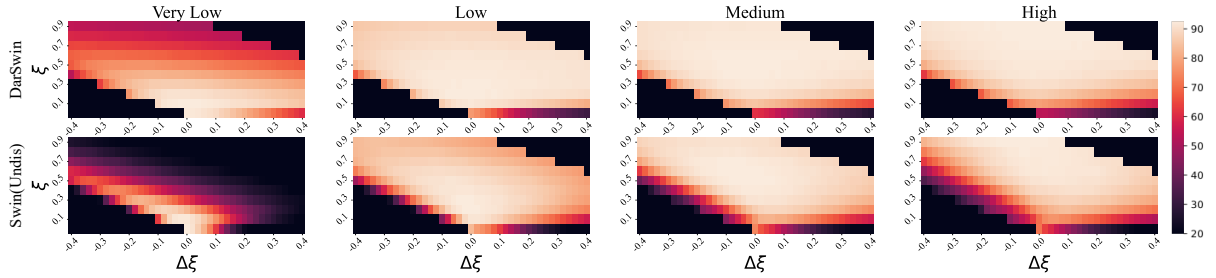


Fig. 8: Sensitivity analysis to errors in lens distortion parameter ξ . Each plot shows the color-coded mean top-1 classification accuracy (brighter is better). For each plot, the x and y axes represent the error $\Delta\xi$ and the ground truth in distortion parameter ξ respectively given to DarSwin (top row) and Swin(undis) (bottom row) during evaluation. Columns correspond to different distortion levels (from Very Low to High) used during training.

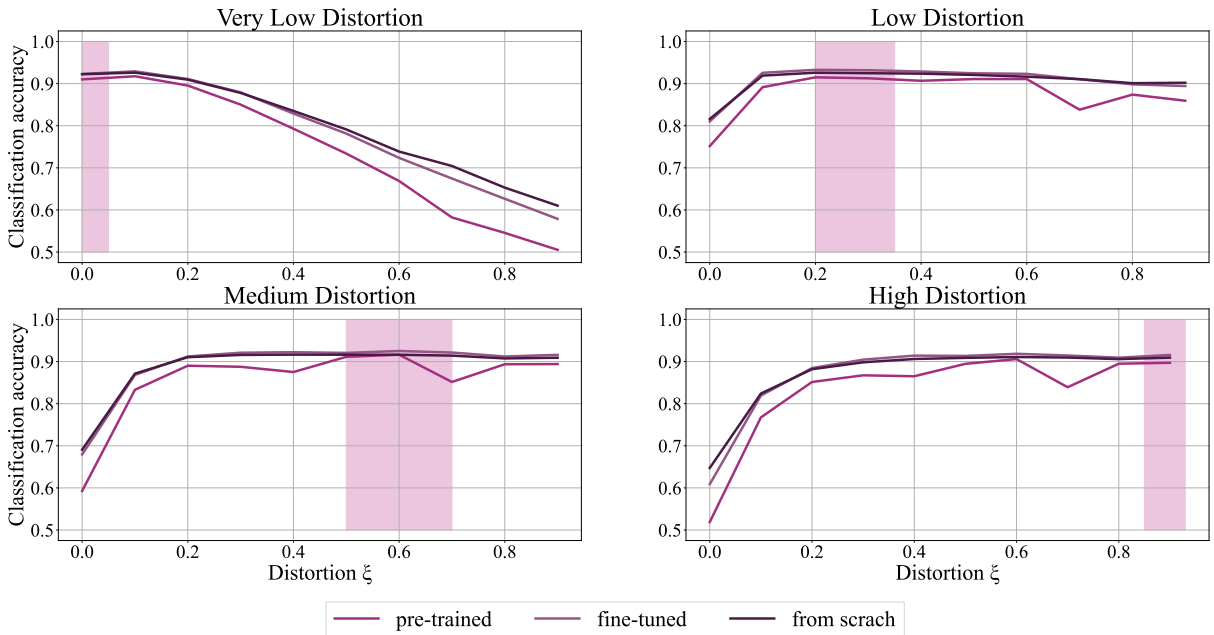


Fig. 9: Results for the self-calibration experiments, where the lens distortion parameter ξ is provided, at test time, by a separate calibration network. We compare three training scenarios for DarSwin: trained on ground truth ξ (“pre-trained”), trained on ground truth ξ then fine-tuned on predictions from the calibration network (“fine-tuned”), and trained from scratch on predictions from the calibration network (“from scratch”).

The output layer uses the softmax activation function on 256 outputs, which correspond to a uniform binning of the $[0, 1]$ interval. We employ the cross entropy loss on all outputs and train the model using the Adam optimizer. We train this network on the ImageNet1k train set by distorting the images on the fly through uniform sampling $\xi \in [0, 1]$.

Self-calibration experiments

We perform three sets of experiments and report results in fig. 9. In all cases, DarSwin is provided with the lens distortion parameter ξ predicted by the calibration network at test time. We experiment with three training scenarios where DarSwin is trained: 1) on ground truth ξ exclusively; 2) on ground truth ξ then fine-tuned on

predictions from the calibration network; and 3) from scratch on predictions from the calibration network.

We observe in fig. 9 that while all scenarios perform similarly within the training region, both the “fine-tuned” and “from scratch” markedly better in generalization. Indeed, adapting DarSwin to the predictions of the calibration network helps, as expected. There does not seem to be a noticeable difference between “fine-tuned” and “from scratch”, however. This last result shows that DarSwin can be trained on uncalibrated wide-angle images, provided a robust calibration network is available (such as [72] for example).

5.6 Ablations

We ablate some important design elements (tab. 3) and training strategies (tab. 4). All ablations are performed using DarSwin-A trained on the “low” distortion ($\xi \in [0.2, 0.35]$) and tested on all the distortion levels.

Positional encoding (PE)

We compare our angular relative positional encoding (sec. 4.5) with two versions of the Fourier-based polar positional encoding from [74] in the first part of tab. 3. First, polar PE encodes patches using their relative distortion-aware radial lengths r and azimuth values φ . Second, angular PE encodes patches using the relative value of incident angle θ and azimuth φ . While angular PE yields better performance, we observe that our angular relative PE improves the performance even further.

Number of sampling points along radius N_{sr}

From N_s sampling points in DarSwin and N_{sr} defining number of sampling points along radius. We observe in tab. 3 that, with $N_{sr} = 10$ sampling points along the radius outperforms the models with $N_{sr} = 5$ and $N_{sr} = 2$ sampling points along the radius by just over (1-6)%.

Window formations and merging

Ablations of different window formation and merging strategies : along azimuth (DarSwin-A) or along radius+azimuth (DarSwin-RA) respectively are reported in tab. 3. We observe that merging along the azimuth outperforms the merging along radius+azimuth by approximately (1-4)% on each distortion level.

	Very low	Low	Medium	High
Ang. rel. PE	83.4%	92.8%	91.5%	88.3%
Polar PE [74]	79.6%	92.0%	90.1%	85.4%
Ang. PE [74]	81.5%	92.6%	91.1%	87.4%
$N_{sr} = 10$	83.4%	92.8%	91.5%	88.3%
$N_{sr} = 5$	81.8%	92.0%	90.0%	85.2%
$N_{sr} = 2$	78.9%	90.4%	87.9%	82.4%
DarSwin-A	83.4%	92.8%	91.5%	88.3%
DarSwin-RA	79.7%	92.7%	90.3%	84.7%

Table 3: Ablation study on different design elements of DarSwin, including different positional encodings, number of sampling points along the radius S_r , and window formation and merging strategy: DarSwin-A (azimuth) or DarSwin-RA (radius+azimuth).

Table 4: Ablation study on different types of sampling techniques and augmentation strategies on DarSwin-A. For jittering we compare “no jitter” (all samples are given to the MLP for linear embedding as is) with “with jitter” (jittering is applied). For sampling, we compare “Unif. sampl.”: points are sampled uniformly inside a patch; to “Distortion aware (DA) sampl.”: lens information is taken into account to sample points inside a patch. “Distortion aware (DA) part.” DarSwin uses lens information to partition the patch.

	Very low	Low	Medium	High
With jitter	83.4%	92.8%	91.5%	88.3%
No jitter	81.5%	92.6%	91.2%	87.4%
DA sampl.	83.4%	92.8%	91.5%	88.3%
Unif. sampl.	82.4%	92.5%	91.2%	86.2%
DA part.	83.4%	92.8%	91.5%	88.3%
w/o DA part.	52.2%	91.3%	86.2%	75.5%

Jittering

When patches are sampled for the linear embedding layer (c.f. sec. 4.3), an augmentation strategy is used to jitter the sample points in the patch. According to tab. 4, this jittering augmentation improves the performance by (1-2)%.

Distortion aware (DA) sampling.

We observe in tab. 4 that distortion aware sampling improves performance by almost (2-6)% compared to uniform sampling in a patch.

Table 5: Comparison of our method with baselines on generalization across projection model. We record top-1 accuracy on the polynomial projection test set for all methods trained on four distortion levels of the spherical projection model. Each row is color-coded as best and second best.

	Very Low	Low	Medium	High
Swin(undis)	85.9%	87.1%	71.3%	60.3%
DAT	65.4%	85.9%	78.9%	63.8%
Swin	33.5%	70.2%	42.3%	25.6%
DarSwin	82.7%	84.8%	78.4%	65.5%

Distortion aware (DA) patch partition.

We observe in tab. 4 that without lens information, DarSwin cannot generalize to unseen distortion.

5.7 Generalization over projection models

In tab. 5, we aim to check for robustness to domain shift at inference due to the use of a different distortion model (c.f. sec. 3). In particular, we use the test set of 30,000 images and distort them using the distortion parameters of a 4-degree polynomial projection model. Each image in the test set is assigned four different distortion parameters randomly sampled from a uniform distribution. The undistortion is not exact since the polynomial projection function is not invertible. Hence Swin(undis) performs only better than DarSwin on low distortions, but the performance degrades on medium to high distortion levels. Our model performs better generalization on all distortion levels. DAT fails to generalize on low distortion levels, and Swin (undis) fails to generalize on high distortions.

6 Depth estimation experiments

We now experiment with our full distortion-aware encoder-decoder architecture (DarSwin-Unet) from fig. 2. Monocular depth estimation is considered as target task for this purpose, since it is a pixel-level regression problem that is inherently ill-posed and ambiguous because many 3D scenes can be projected to the same 2D image. The problem also becomes more complex with the significant distortion in fish-eye images. Experiments provided in this section confirm the previous findings about DarSwin’s promising generalization abilities and show that they apply for pixel-level tasks as well. In this section, we will

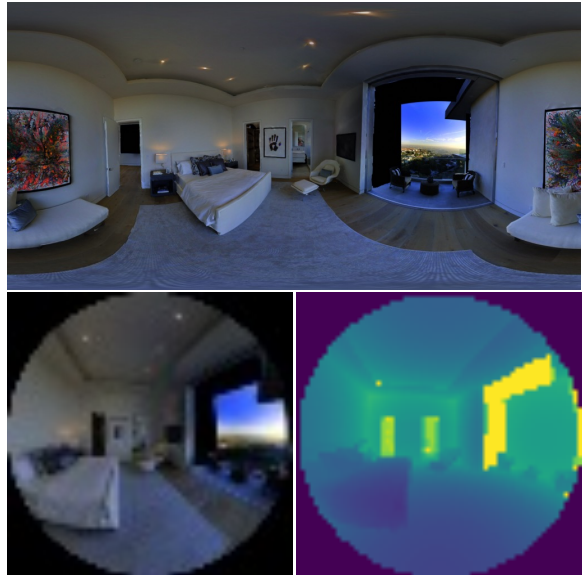


Fig. 10: From an input RGB panorama (top) with corresponding depth map (not shown) from the Matterport3D dataset [75], we generate a wide angle image and its depth map (bottom). Here, the field of view is 175° and $\xi = 0.95$.

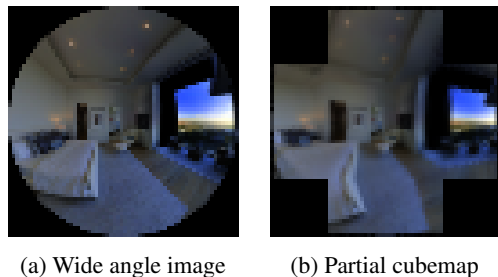


Fig. 11: Cubemap generation: we warp the (a) 175° wide angle image to the corresponding (b) partial cubemap representation.

refer to our method as DarSwin-Unet to emphasize its encoder-decoder structure.

6.1 Datasets

Since existing wide-angle depth estimation datasets such as Woodscapes [4] do not provide a wide range of distortion profiles to understand the generalization capacity of our network, we instead simulate a wide range of lenses using the same spherical model (c.f. sec. 3) on the indoor Matterport3D dataset [75] as illustrated in fig. 10. Note that this warping can easily be

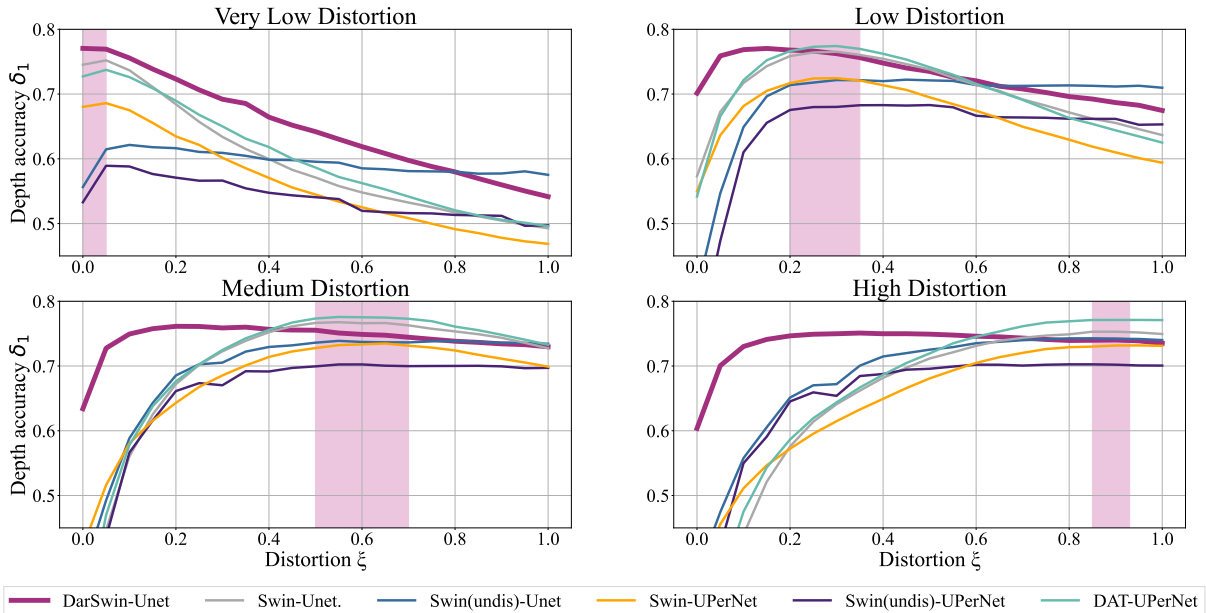


Fig. 12: Depth estimation accuracy δ_1 (higher is better) as a function of test distortion for: DarSwin-UNET, Swin-UNET [27], Swin(undis)-UNET, Swin-UPerNet [5, 76], Swin(undis)-UPerNet and DAT-UPerNet [25, 76]. All methods are trained on a restricted set of lens distortion curves (indicated by the pink shaded regions): (a) Very low, (b) low, (c) medium and (d) high distortion. We study the generalization abilities of each model by testing across all $\xi \in [0, 1]$.

done since the spherical projection model (c.f. sec. 3) allows a closed-form solution to its inverse projection.

Training set

Similar to the classification experiments (sec. 5.1), we generate four different training sets with the same levels of distortion. Training images are synthetically generated from panoramas on the fly during training with distortion ξ sampled from their respective intervals and the yaw viewing angle being uniformly sampled in the $[0, 360^\circ]$ interval. Each of the four training set (one for each distortion group) contains 9180 panoramas of original resolution of 512×1024 , where the generated wide-angle image is subsequently downsampled to 64×64 after warping.

Test set

To evaluate zero-shot generalization to lens distortions, we generate wide-angle images from the test set containing 1620 panoramas, for every ξ in uniform discrete distribution $[0, 1]$ with step size 10.

6.2 Baselines and training details

We compare DarSwin-UNET with the following baselines: Swin-UNET [27], Swin-UPerNet (a Swin [5]

encoder with UPerNet [76] decoder) and DAT-UPerNet (a DAT [25] encoder with UPerNet decoder). As with classification (sec. 5), we also wish to compare against models trained on undistorted images. Here, we include two such additional baselines: Swin-UNET(undis) and Swin-UPerNet(undis).

Undistortion-piecewise linear correction

Undistorting a 175° field-of-view wide angle image to a single perspective image will result in extremely severe stretching. Instead, we follow the piecewise linear correction strategy in [4] and undistort the image to a partial cubemap, which is composed of 6 perspective faces of 90° field of view each, unrolled into an image. As shown in fig. 11, this preserves the entire field of view while minimizing stretching. These images are used to train the “(undis)” baselines mentioned above.

Training details

All baselines employ 32 divisions along the image width and height. For DarSwin-UNET, we use $N_r = 16$ and $N_\phi = 64$ divisions along the radius and azimuth respectively, which yields the same number of 4096 patches for image size 64×64 . All three baselines are

trained with a window size (4, 4) and DarSwin-Unet is trained with window size (1, 16).

All encoders (Swin and DAT) are first pre-trained for classification on the distorted ImageNet1K dataset from sec. 5.1. Pre-trained encoders are then fine-tuned, along with their respective decoders, on the depth estimation task.

All methods are trained with the SGD optimizer with momentum 0.9 and weight decay 1e-4 on a batch size of 8. We employ a polynomial learning rate policy with a base learning rate of 0.01 and power = 0.9. We use random flips and rotations as data augmentation.

Training loss

Since the global scale of a scene is a fundamental ambiguity in depth estimation [77], we train the network using the *scale-invariant loss* in log space [78]:

$$L = \sqrt{\frac{1}{n} \sum_i d_i^2 - \frac{\lambda}{n^2} (\sum_i d_i)^2}, \quad (12)$$

with d_i is the difference between the predicted and ground truth (log-)depth. We use $\lambda = 0.85$.

Evaluation metrics

We evaluate performance on typical depth estimation metrics [78]: absolute relative error, RMSE, log-RMSE, squared relative error and accuracy under threshold ($\delta_i, i \in \{1, 2, 3\}$). The paper reports results on

$$\delta_1 = \frac{1}{|D|} |\{d \in D \mid \max(\frac{d^*}{d}, \frac{d}{d^*}) \leq 1.25\}|, \quad (13)$$

where D, d^* and d are the set of valid, ground truth and predicted depths respectively. Please consult the supplementary material for other metrics.

6.3 Zero-shot generalization

As with the classification experiments (sec. 5.3), we train each approach on a specific distortion level (c.f. sec. 5.1) and evaluate them on all distortion values $\xi \in [0, 1]$. Fig. 12 illustrates the results using the accuracy δ_1 metric. Overall, we observe that DarSwin-Unet maintains the most stable performance as we move away from the training distortion for all levels of training distortions. We note that Swin(undis)-Unet has competitive performance when the test distortion is greater than the one used for training. However, its performance severely drops in the opposite scenario (visible in the Low, Medium and High distortion

figures). We also observe that the performance of DarSwin-Unet when the test distortion is equal to training (indicated by the shaded regions) is somewhat lower than other baselines (all cases except the Very Low training distortion): DAT-UperNet is the best-performing method in this case. However, its performance in generalization outside the training distortion severely drops, indicating that it cannot adapt to other lenses at test time.

7 Discussion

This paper presents DarSwin, a new distortion aware vision transformer which adapts its structure to the lens distortion profile of a (calibrated) lens. DarSwin achieves state-of-the-art performance on zero-shot adaptation (without pretraining) on different lenses on classification using synthetically distorted images from the ImageNet1k dataset.

While the original DarSwin idea was introduced in [26], this paper presents three new contributions, significantly extending the DarSwin encoder-only architecture. First, a self-calibration network is used to calibrate the lens profile, resulting in an entirely uncalibrated pipeline for wide-angle image recognition. Second, DarSwin-Unet is an extension of DarSwin encoder to a full encoder-decoder distortion-aware architecture. Third, we demonstrate that DarSwin-Unet achieves state-of-the-art performance on zero-shot adaptation (without pretraining) on different lenses for per-pixel depth estimation using synthetically distorted images from the Matterport3D datasets, respectively.

Limitations and future research directions

Despite strong generalization capabilities, our method still has limitations that should be explored in future work. First, while the distortion-aware sampling strategy was shown to be effective for zero-shot adaptation, the sparsity of sampling points and the necessity to interpolate pixel values may affect the performance of the model. While this issue is partially alleviated using our proposed jittering augmentation technique, other strategies may also be possible. This is also a problem in per-pixel tasks such as depth estimation, which must rely on a k -NN for mapping the samples back to pixel space. Second, our model assumes knowledge of the lens distortion profile; hence, it is appropriate only for the calibrated case. For the classification experiment, as shown in the above section, we took inspiration

from [72] to calibrate the uncalibrated lens using a network. However, the limitation persists for the depth estimation task.

References

- [1] Kim, H., Chae, E., Jo, G., Paik, J.: Fisheye lens-based surveillance camera for wide field-of-view monitoring. In: IEEE Int. Conf. Cons. Elec. (2015)
- [2] Schmalstieg, D., Hiller, T.: Augmented reality: Principles and practice. In: IEEE Virt. Reality (2017)
- [3] Deng, L., Yang, M., Li, H., Li, T., Bing, h., Wang, C.: Restricted deformable convolution-based road scene semantic segmentation using surround view cameras. IEEE Trans. Int. Trans. Syst. (2019)
- [4] Yogamani, S., Hughes, C., Horgan, J., Sistu, G., Chennupati, S., Uricar, M., Milz, S., Simon, M., Amende, K., Witt, C., Rashed, H., Nayak, S., Mansoor, S., Varley, P., Perrotton, X., Odea, D., Prez, P.: Woodscape: A multi-task, multi-camera fisheye dataset for autonomous driving. In: Int. Conf. Comput. Vis. (2019)
- [5] Liu, Z., Lin, Y., Cao, Y., Hu, H., Wei, Y., Zhang, Z., Lin, S., Guo, B.: Swin transformer: Hierarchical vision transformer using shifted windows. In: Int. Conf. Comput. Vis. (2021)
- [6] Huang, X., Liu, M.-Y., Belongie, S., Kautz, J.: Multimodal unsupervised image-to-image translation. In: Eur. Conf. Comput. Vis. (2018)
- [7] Torralba, A., Efros, A.A.: Unbiased look at dataset bias. In: IEEE Conf. Comput. Vis. Pattern Recog. (2011)
- [8] Khosla, A., Zhou, T., Malisiewicz, T., Efros, A.A., Torralba, A.: Undoing the damage of dataset bias. In: Eur. Conf. Comput. Vis. (2012)
- [9] Brousseau, P.-A., Roy, S.: Calibration of axial fisheye cameras through generic virtual central models. In: Int. Conf. Comput. Vis. (2019)
- [10] Ramalingam, S., Sturm, P.: A unifying model for camera calibration. IEEE Trans. Pattern Anal. Mach. Intell. **39**(7), 1309–1319 (2017)
- [11] Zhang, M., Yao, J., Xia, M., Li, K., Zhang, Y., Liu, Y.: Line-based multi-label energy optimization for fisheye image rectification and calibration. In: IEEE Conf. Comput. Vis. Pattern Recog. (2015)
- [12] Melo, R., Antunes, M., Barreto, J.P., Falco, G., Goncalves, N.: Unsupervised intrinsic calibration from a single frame using a “plumb-line” approach. In: Int. Conf. Comput. Vis. (2013)
- [13] Kannala, J., Brandt, S.S.: A generic camera model and calibration method for conventional, wide-angle, and fish-eye lenses. IEEE Trans. Pattern Anal. Mach. Intell. **22**(8), 1335–1340 (2006)
- [14] Yin, X., Wang, X., Yu, J., Zhang, M., Fua, P., Tao, D.: Fisheyerecnet: A multi-context collaborative deep network for fisheye image rectification. In: Eur. Conf. Comput. Vis. (2018)
- [15] Xue, Z., Xue, N., Xia, G., Shen, W.: Learning to calibrate straight lines for fisheye image rectification. In: IEEE Conf. Comput. Vis. Pattern Recog. (2019)
- [16] Plaut, E., Ben Yaacov, E., El Shlomo, B.: 3d object detection from a single fisheye image without a single fisheye training image. In: IEEE Conf. Comput. Vis. Pattern Recog. Worksh. (2021)
- [17] Ployart, C., Ahmad, O., Lécué, F., Cheriet, F.: Adaptable deformable convolutions for semantic segmentation of fisheye images in autonomous driving systems. CoRR **abs/2102.10191** (2021)
- [18] Ahmad, O., Lecue, F.: FisheyeHDK: Hyperbolic deformable kernel learning for ultra-wide field-of-view image recognition. In: AAAI (2022)
- [19] Dai, J., Qi, H., Xiong, Y., Li, Y., Zhang, G., Hu, H., Wei, Y.: Deformable convolutional networks. In: Int. Conf. Comput. Vis. (2017)
- [20] Zhu, X., Hu, H., Lin, S., Dai, J.: Deformable convnets v2: More deformable, better results. In: IEEE Conf. Comput. Vis. Pattern Recog. (2019)
- [21] Cohen, T.S., Geiger, M., Köhler, J., Welling, M.: Spherical cnns. In: Int. Conf. Learn. Represent. (2018)
- [22] Cohen, T.S., Weiler, M., Kicanaoglu, B., Welling,

- M.: Gauge equivariant convolutional networks and the icosahedral CNN. In: *Int. Conf. on Mach. Learning* (2019)
- [23] Dosovitskiy, A., Beyer, L., Kolesnikov, A., Weissenborn, D., Zhai, X., Unterthiner, T., Dehghani, M., Minderer, M., Heigold, G., Gelly, S., Uszkoreit, J., Houlsby, N.: An image is worth 16x16 words: Transformers for image recognition at scale. In: *Int. Conf. Learn. Represent.* (2020)
- [24] Zhou, D., Kang, B., Jin, X., Yang, L., Lian, X., Hou, Q., Feng, J.: Deepvit: Towards deeper vision transformer. *arXiv preprint arXiv:2103.11886* (2021)
- [25] Xia, Z., Pan, X., Song, S., Li, L.E., Huang, G.: Vision transformer with deformable attention. In: *IEEE Conf. Comput. Vis. Pattern Recog.* (2022)
- [26] Athwale, A., Afrasiyabi, A., Lagüe, J., Shili, I., Ahmad, O., Lalonde, J.-F.: Darswin: Distortion aware radial swin transformer. In: *Int. Conf. Comput. Vis.* (2023)
- [27] Cao, H., Wang, Y., Chen, J., Jiang, D., Zhang, X., Tian, Q., Wang, M.: Swin-Unet: Unet-like Pure Transformer for Medical Image Segmentation (2021)
- [28] Xiong, Y., Liao, R., Zhao, H., Hu, R., Bai, M., Yumer, E., Urtasun, R.: UPSNet: A Unified Panoptic Segmentation Network (2019)
- [29] Zioulis, N., Karakottas, A., Zarpalas, D., Daras, P.: Omnidepth: Dense depth estimation for indoors spherical panoramas. In: *Eur. Conf. Comput. Vis.* (2018)
- [30] Yun, H., Lee, S., Kim, G.: Panoramic vision transformer for saliency detection in 360° videos. In: *Eur. Conf. Comput. Vis.* (2022)
- [31] Zhang, J., Yang, K., Ma, C., Reiß, S., Peng, K., Stiefelhagen, R.: Bending reality: Distortion-aware transformers for adapting to panoramic semantic segmentation. In: *IEEE Conf. Comput. Vis. Pattern Recog.* (2022)
- [32] Fernandez-Labrador, C., Perez-Yus, A., Lopez-Nicolas, G., Guerrero, J.J.: Layouts from panoramic images with geometry and deep learning. *IEEE Rob. Autom. Letters* **3**(4), 3153–3160 (2018)
- [33] Su, Y.-C., Grauman, K.: Kernel transformer networks for compact spherical convolution. In: *IEEE Conf. Comput. Vis. Pattern Recog.* (2019)
- [34] Rashed, H., Mohamed, E., Sistu, G., Kumar, V.R., Eising, C., El-Sallab, A., Yogamani, S.: Generalized object detection on fisheye cameras for autonomous driving: Dataset, representations and baseline. In: *Wint. Conf. Appl. Comput. Vis.* (2021)
- [35] Rashed, H., Mohamed, E., Sistu, G., Ravi Kumar, V., Eising, C., Sallab, A., Yogamani, S.: Fisheyeyolo: Object detection on fisheye cameras for autonomous driving. In: *Adv. Neural Inform. Process. Syst.* (2020)
- [36] Ye, Y., Yang, K., Xiang, K., Wang, J., Wang, K.: Universal semantic segmentation for fisheye urban driving images. *IEEE Int. Conf. Syst. Man Cyber.*, 648–655 (2020)
- [37] Kumar, V.R., Yogamani, S., Rashed, H., Sitsu, G., Witt, C., Leang, I., Milz, S., Mäder, P.: Omnidet: Surround view cameras based multi-task visual perception network for autonomous driving. *IEEE Robot. Autom. Letters* **6**(2), 2830–2837 (2021)
- [38] Kumar, V.R.: Surround-view cameras based holistic visual perception for automated driving. *IEEE Transa. on Int. Transport. Sys.* (2022)
- [39] Liao, Y., Xie, J., Geiger, A.: Kitti-360: A novel dataset and benchmarks for urban scene understanding in 2d and 3d. *IEEE Trans. Pattern Anal. Mach. Intell.* (2022)
- [40] Devernay, F., Faugeras, O.: Straight lines have to be straight automatic calibration and removal of distortion from scenes of structured environments. *Mach. Vis. Appl.* **13** (2001)
- [41] Kim, B., Lee, D., Min, K., Chong, J., Joe, I.: Global convolutional neural networks with self-attention for fisheye image rectification. *IEEE Access* **10**, 129580–129587 (2022) <https://doi.org/10.1109/ACCESS.2022.3228297>

- [42] Liao, K., Lin, C., Zhao, Y., Xu, M.: Model-free distortion rectification framework bridged by distortion distribution map. *IEEE Trans. Image Process.* **29**, 3707–3718 (2020)
- [43] Liao, K., Lin, C., Zhao, Y.: A deep ordinal distortion estimation approach for distortion rectification. *IEEE Trans. Image Process.* **30**, 3362–3375 (2021)
- [44] Yang, S., Lin, C., Liao, K., Zhang, C., Zhao, Y.: Progressively complementary network for fish-eye image rectification using appearance flow. In: *IEEE Conf. Comput. Vis. Pattern Recog.* (2021)
- [45] Feng, H., Wang, W., Deng, J., Zhou, W., Li, L., Li, H.: Simfir: A simple framework for fisheye image rectification with self-supervised representation learning. In: *Int. Conf. Comput. Vis.* (2023)
- [46] Yang, S., Lin, C., Liao, K., Zhao, Y.: Dual Diffusion Architecture for Fisheye Image Rectification: Synthetic-to-Real Generalization (2023)
- [47] Yang, S., Lin, C., Liao, K., Zhao, Y.: Fishformer: Annulus slicing-based transformer for fisheye rectification with efficacy domain exploration. *arXiv preprint arXiv:2207.01925* (2022)
- [48] Krizhevsky, A., Sutskever, I., Hinton, G.E.: Imagenet classification with deep convolutional neural networks. In: *Adv. Neural Inform. Process. Syst.* (2012)
- [49] Szegedy, C., Liu, W., Jia, Y., Sermanet, P., Reed, S.E., Anguelov, D., Erhan, D., Vanhoucke, V., Rabinovich, A.: Feature pyramid networks for object detection. In: *IEEE Conf. Comput. Vis. Pattern Recog.* (2015)
- [50] Liu, S., Deng, W.: Very deep convolutional neural network based image classification using small training sample size. In: *2015 3rd IAPR Asian Conference on Pattern Recognition (ACPR)* (2015)
- [51] Bronstein, M.M., Bruna, J., Cohen, T., Velickovic, P.: Geometric deep learning: Grids, groups, graphs, geodesics, and gauges. *CoRR abs/2104.13478* (2021) [2104.13478](https://arxiv.org/abs/2104.13478)
- [52] Sez, ., Bergasa, L.M., Romeral, E., Lpez, E., Barea, R., Sanz, R.: Cnn-based fisheye image real-time semantic segmentation. In: *2018 IEEE Intelligent Vehicles Symposium (IV)* (2018)
- [53] Yan, Q., Ji, P., Bansal, N., Ma, Y., Tian, Y., Xu, Y.: FisheyeDistill: Self-Supervised Monocular Depth Estimation with Ordinal Distillation for Fisheye Cameras (2021)
- [54] Kumar, V.R., Yogamani, S., Rashed, H., Sitsu, G., Witt, C., Leang, I., Milz, S., Mäder, P.: Omninet: Surround view cameras based multi-task visual perception network for autonomous driving. *IEEE Robotics and Automation Letters* **6**(2), 2830–2837 (2021)
- [55] Kumar, V.R., Klingner, M., Yogamani, S., Milz, S., Fingscheidt, T., Mader, P.: Syndistnet: Self-supervised monocular fisheye camera distance estimation synergized with semantic segmentation for autonomous driving. In: *Wint. Conf. Appl. Comput. Vis.* (2021)
- [56] Kumar, V.R., Klingner, M., Yogamani, S., Bach, M., Milz, S., Fingscheidt, T., Mäder, P.: Svdistnet: Self-supervised near-field distance estimation on surround view fisheye cameras. *IEEE Transactions on Intelligent Transportation Systems* **23**(8), 10252–10261 (2021)
- [57] Wei, X., Ran, Z., Lu, X.: Dcpb: Deformable convolution based on the poincare ball for top-view fisheye cameras. In: *Int. Conf. Comput. Vis.* (2023)
- [58] Vaswani, A., Shazeer, N., Parmar, N., Uszkoreit, J., Jones, L., Gomez, A.N., Kaiser, Ł., Polosukhin, I.: Attention is all you need. In: *Adv. Neural Inform. Process. Syst.* (2017)
- [59] Zhang, J., Yang, K., Shi, H., Rei, S., Peng, K., Ma, C., Fu, H., Torr, P.H.S., Wang, K., Stiefelhagen, R.: Behind Every Domain There is a Shift: Adapting Distortion-aware Vision Transformers for Panoramic Semantic Segmentation (2022)
- [60] Lee, J., Cho, G., Park, J., Kim, K., Lee, S., Kim, J.-H., Jeong, S.-G., Joo, K.: Slabins: Fish-eye depth estimation using slanted bins on road environments. In: *Int. Conf. Comput. Vis.* (2023)
- [61] Shi, H., Li, Y., Yang, K., Zhang, J., Peng, K.,

- Roitberg, A., Ye, Y., Ni, H., Wang, K., Stiefelhaugen, R.: Fishdreamer: Towards fisheye semantic completion via unified image outpainting and segmentation (2023)
- [62] Kumar, V.R., Hiremath, S.A., Milz, S., Witt, C., Pinnard, C., Yogamani, S., Mader, P.: FisheyeDistanceNet: Self-Supervised Scale-Aware Distance Estimation using Monocular Fisheye Camera for Autonomous Driving (2020)
- [63] Kumar, V.R., Yogamani, S., Bach, M., Witt, C., Milz, S., Mader, P.: UnRectDepthNet: Self-Supervised Monocular Depth Estimation using a Generic Framework for Handling Common Camera Distortion Models (2023)
- [64] Beck, C.: Apparatus to photograph the whole sky. *J. Scientific Inst.* **2**(4), 135–139 (1925)
- [65] Hill, R.: A lens for whole sky photographs. *Quart. J. Royal Meteor. Soc.* **50**(211), 227–235 (1924)
- [66] Fleck, M.M.: Perspective projection: The wrong imaging model. *IEEE Trans. Reliability* (1995)
- [67] Miyamoto, K.: Fish eye lens. *J. Opt. Soc. Am.* **54**(8), 1060–1061 (1964) <https://doi.org/10.1364/JOSA.54.001060>
- [68] Hughes, C., Denny, P., Jones, E., Glavin, M.: Accuracy of fish-eye lens models. *Applied optics* **49**(17), 3338–3347 (2010)
- [69] Barreto, J.P.: A unifying geometric representation for central projection systems. *Comput. Vis. Img. Underst.* (2006)
- [70] Mei, C., Rives, P.: Single view point omnidirectional camera calibration from planar grids. In: *Int. Conf. Robot. Aut.* (2007)
- [71] Ying, X., Hu, Z.: Can we consider central catadioptric cameras and fisheye cameras within a unified imaging model. In: *Eur. Conf. Comput. Vis.* (2004)
- [72] Hold-Geoffroy, Y., Piché-Meunier, D., Sunkavalli, K., Bazin, J.-C., Rameau, F., Lalonde, J.-F.: A perceptual measure for deep single image camera and lens calibration. *IEEE Transactions on Pattern Analysis and Machine Intelligence* **45**(9) (2023)
- [73] Liu, Z., Mao, H., Wu, C.-Y., Feichtenhofer, C., Darrell, T., Xie, S.: A ConvNet for the 2020s (2022)
- [74] Ning, K., Xie, L., Wu, F., Tian, Q.: Polar relative positional encoding for video-language segmentation. In: *Int. Joint Conf. Art. Intel.* (2020)
- [75] Chang, A., Dai, A., Funkhouser, T., Halber, M., Niessner, M., Savva, M., Song, S., Zeng, A., Zhang, Y.: Matterport3d: Learning from rgb-d data in indoor environments. *International Conference on 3D Vision (3DV)* (2017)
- [76] Xiao, T., Liu, Y., Zhou, B., Jiang, Y., Sun, J.: Unified perceptual parsing for scene understanding. In: *Eur. Conf. Comput. Vis.* (2018)
- [77] Eigen, D., Puhrsch, C., Fergus, R.: Depth map prediction from a single image using a multi-scale deep network. *Adv. Neural Inform. Process. Syst.* (2014)
- [78] Shu, C., Chen, Z., Chen, L., Ma, K., Wang, M., Ren, H.: Sidert: A real-time pure transformer architecture for single image depth estimation. *arXiv preprint arXiv:2204.13892* (2022)